AIP Journal of Applied Physics

Thermoelectric transport properties of diamond-like Cu1−xFe1+xS2 tetrahedral compounds

Yulong Li, Tiansong Zhang, Yuting Qin, Tristan Day, G. Jeffrey Snyder, Xun Shi, and Lidong Chen

Citation: Journal of Applied Physics **116**, 203705 (2014); doi: 10.1063/1.4902849
View online: http://dx.doi.org/10.1063/1.4902849
View Table of Contents: http://scitation.aip.org/content/aip/journal/jap/116/20?ver=pdfcov
Published by the AIP Publishing

JOURNAL OF APPLIED PHYSICS **116**, 203705 (2014)

Thermoelectric transport properties of diamond-like $Cu_{1-x}Fe_{1+x}S_2$ tetrahedral compounds

Yulong Li,[1,2,3] Tiansong Zhang,[1,2] Yuting Qin,[1,2,3] Tristan Day,[4] G. Jeffrey Snyder,[4] Xun Shi,[1,2,a)] and Lidong Chen[1,2,a)]

[1]*State Key Laboratory of High Performance Ceramics and Superfine Microstructure, Shanghai Institute of Ceramics, Chinese Academy of Sciences, Shanghai 200050, China*
[2]*CAS Key Laboratory of Materials for Energy Conversion, Shanghai Institute of Ceramics, Chinese Academy of Sciences, Shanghai 200050, China*
[3]*University of Chinese Academy of Sciences, Beijing 100049, China*
[4]*Department of Materials Science, California Institute of Technology, Pasadena, California 91125, USA*

(Received 4 September 2014; accepted 15 November 2014; published online 26 November 2014)

Polycrystalline samples with the composition of $Cu_{1-x}Fe_{1+x}S_2$ (x = 0, 0.01, 0.03, 0.05, 0.1) were synthesized by a melting-annealing-sintering process. X-ray powder diffraction reveals all the samples are phase pure. The backscattered electron image and X-ray map indicate that all elements are distributed homogeneously in the matrix. The measurements of Hall coefficient, electrical conductivity, and Seebeck coefficient show that Fe is an effective n-type dopant in $CuFeS_2$. The electron carrier concentration of $Cu_{1-x}Fe_{1+x}S_2$ is tuned within a wide range leading to optimized power factors. The lattice phonons are also strongly scattered by the substitution of Fe for Cu, leading to reduced thermal conductivity. We use Debye approximation to model the low temperature lattice thermal conductivity. It is found that the large strain field fluctuation introduced by the disordered Fe ions generates extra strong phonon scatterings for lowered lattice thermal conductivity. © *2014 AIP Publishing LLC*. [http://dx.doi.org/10.1063/1.4902849]

I. INTRODUCTION

Thermoelectric materials have attracted extensive attention due to the potential applications in heat pumping and power generation.[1,2] The performance of thermoelectric materials is determined by the dimensionless thermoelectric figure of merit $zT = \alpha^2\sigma T/\kappa$, where α is the Seebeck coefficient, σ is the electrical conductivity, T is the absolute temperature, and κ is the thermal conductivity. The strategy of maximizing zT is to obtain large power factor ($\alpha^2\sigma$) as well as low thermal conductivity.[3] Advanced thermoelectric materials including Bi_2Te_3,[4] PbTe,[5,6] skutterudites,[7,8] clathrates,[9] Cu_2X (X = S, Se),[10,11] etc., have been continually discovered and investigated to enhance the zTs. In particular, in order to meet industry requirements, the high performance earth-abundant, low-cost, nontoxic, and environmentally benign thermoelectric materials have drawn lots of attention recently.[2,11,12]

A family of compounds with diamond-like structure, such as $Cu_2ZnSn_{1-x}In_xSe_4$, $Cu_2Sn_{1-x}In_xSe_3$, $CuInTe_2$, and $CuGaTe_2$,[13–16] has emerged as promising thermoelectric materials in the past few years. The diamond-like compounds derive from binary cubic zinc-blende compounds by using various elements substituted at Zn sites. Due to the different physical and chemical properties of the substituted elements at Zn sites, the crystal lattice is distorted from the perfectly cubic diamond lattice to lower the lattice thermal conductivity. By combining the optimization of electrical properties, the zTs up to 1.2–1.4 are reported in current diamond-like compounds. These high zT values are mainly realized in the tetrahedral compounds such as $CuInTe_2$ and $CuGaTe_2$. By using first principle calculations, Zhang *et al.* did a systemic study on the tetrahedral diamond-like compounds.[17] An effective unity-η rule is proposed to explain the current high zTs in $CuInTe_2$, $CuGaTe_2$, and $Cu_2ZnSn_{1-x}In_xSe_4$, where $\eta = c/2a$, and c and a are lattice parameters. When η is around 1, the crystal field splitting energy reaches the minimum state, leading to a cubic-like highly degenerate electronic band-edge state for large power factors and high zT values. This unity-η rule can also be used to predict and search for novel tetrahedral non-cubic thermoelectric materials, in particular for those diamond-like materials with similar crystal structures.

Chalcopyrite ore $CuFeS_2$ composed of earth-abundant, non-toxic, and inexpensive elements Cu, Fe, and S, is also a diamond-like compound with tetrahedral structure. The experimental lattice parameters are 10.42 Å for c and 5.289 Å for a. The calculated η value in $CuFeS_2$ is 0.985, which shows a larger deviation than those in $CuInTe_2$ and $CuGaTe_2$, but still quite close to 1. This suggests that $CuFeS_2$ might possess good electrical properties as well as thermoelectric figure of merit since the lattice thermal conductivity is usually low in these diamond-like compounds. $CuFeS_2$ is a narrow band gap semiconductor with a gap (E_g) of 0.53 eV by optical absorption measurement or 0.3 eV by the calculation using spin-polarized self-consistent charge discrete-variational $X\alpha$ method.[18,19] A Seebeck coefficient −480 μV/K and a carrier concentration 10^{19} cm^{-3} at room temperature are reported.[20,21] These data confirmed that $CuFeS_2$ is a good semiconductor within the range of heavily doped materials, and these are particularly suitable for advanced thermoelectric materials.

$CuFeS_2$ with stoichiometric chemical composition is an intrinsic semiconductor with poor power factors. The carrier

a)Electronic addresses: xshi@mail.sic.ac.cn and cld@mail.sic.ac.cn

concentration must be tuned to the optimum value for thermoelectric performance. Li *et al.* used S deficiency to increase carrier concentrations in $CuFeS_{2-x}$ to approach the optimum value, leading to enhanced power factors.[22] A decreased thermal conductivity is also obtained by the enhanced phonon-interface scattering. A maximum zT value of 0.21 was obtained at 573 K for $CuFeS_{1.80}$. Naohito Tsujii and Takao Mori studied mainly the low temperature thermoelectric properties of carrier-doped $Cu_{1-x}Fe_{1+x}S_2$. They assumed that the strong magnetic moment can affect charge carriers based on the early references, resulting in increased electron effective mass and subsequently high power factors.[23,24] However, the carrier-magnetic moment interactions are expected to be weak or to disappear at high temperatures. Thus the electrical transport at high temperatures in the $CuFeS_2$ compound should be dominated by the material's band structure and carrier concentration. In addition, the lattice defects by the arrangement of Cu and Fe atoms in the material could also affect the heat conduction, in particular for the material $Cu_{1-x}Fe_{1+x}S_2$ with Cu and Fe contents significantly shifted from the stoichiometric ratio. Both of these two factors will obviously affect the thermoelectric properties and should be clarified to fully understand the chalcopyrite ore compound $CuFeS_2$.

In this work, we present a systematic study of the thermoelectric properties of chalcopyrite $Cu_{1-x}Fe_{1+x}S_2$ from liquid helium temperature to 700 K. Significantly improved electrical transport and lowered thermal conductivity are observed to show enhanced zT values. The effect of the excessive Fe substituted at Cu sites in $CuFeS_2$ on the electrical and thermal transport and their physical mechanisms are discussed.

II. EXPERIMENT

Polycrystalline $Cu_{1-x}Fe_{1+x}S_2$ (x = 0, 0.01, 0.03, 0.05, and 0.1) samples were synthesized by a melting-annealing-sintering process. High purity elements Cu (shot, 99.999%), Fe (pieces, 99.99%), and S (pieces, 99.999%) in stoichiometric proportions were sealed in evacuated quartz tubes. The quartz tubes were heated slowly up to 1400 K and stayed at this temperature for 36 h, and then naturally cooled to room temperature. The obtained ingots were ground into fine powders and cold pressed into pellets. The pellets were resealed in quartz tubes and annealed at 800–900 K for 7 days. The resulted materials were reground into powders and then sintered by spark plasma sintering at 800–820 K under a pressure of 60 MPa to obtain densified bulk samples.

The phase, morphology, and chemical compositions of the samples were characterized by powder X-ray diffraction (XRD) analysis (Rigaku, Rint2000, Cu $K\alpha$), scanning electron microscope (SEM), and energy dispersive spectrometer (EDS), respectively.

The measurements of Hall coefficient R_H, electrical conductivity σ, thermal conductivity κ, and Seebeck coefficient α at low temperature (2–300 K) were carried out in a Quantum Design Physics Property Measurement System. The high temperature measurements of electrical conductivity and Seebeck coefficient were performed in the ZEM-3 (ULVAC-RIKO) from 300 to 700 K. The high temperature thermal diffusivity (λ) was measured using the laser flash method in flowing argon atmosphere (NETZSCH LFA 457). The thermal conductivity was calculated from $\kappa = \lambda C_p \rho$, where the Dulong-Petit value of 0.518 J/gK was used for the specific heat capacity (C_p) and the density (ρ) was measured using Archimedes method. The velocity of sound was measured by using a Panametrics NDT 5800 pulser/receiver and 5 MHz and 25 MHz shear and longitudinal transducers from Ultran.

III. RESULTS AND DISCUSSION

A. Structural and compositional characterizations

Figure 1 shows the powder X-ray diffraction patterns for $Cu_{1-x}Fe_{1+x}S_2$ samples. All diffraction peaks are consistent with the standard pattern of tetragonal $CuFeS_2$ (JCPDS No. 65–1573) with the space group of I42d. Impurity phases are not observed in the X-ray diffraction patterns even for the sample with the largest x value (x = 0.1). In order to check the element distribution of this sample in microscopic prospective, the backscattered electron (BSE) image of the polished surface and x-ray map by EDS for sample $Cu_{0.9}Fe_{1.1}S_2$ are shown in Figure 2. Element Cu, Fe, and S are all homogeneously distributed in the samples and no obvious large impurity phases are detected. These data strongly suggest that the Fe atoms can substitute at Cu sites with content up to at least 10%.

The atomic ratio of Fe/Cu by EDS measurements is shown in Table I. Due to the measurement uncertainty or errors, the atomic ratio of Fe/Cu is not ideally equal to the initial atomic ratios in all samples, even for sample $CuFeS_2$. However, the atomic ratio of Fe/Cu increases monotonically with increasing Fe content, which shows the same trend as the designed staring compositions. Therefore, by combining Figs. 1 and 2, and Table I, we conclude that the Fe/Cu atomic ratios in $CuFeS_2$ can be tuned in a certain large composition range such as the composition of $Cu_{0.9}Fe_{1.1}S_2$.

B. High-temperature thermoelectric properties

Figure 3 shows the temperature dependence of electrical conductivity (σ) and Seebeck coefficient (α) for all the samples. As Fe doping on the Cu site, the value of electrical

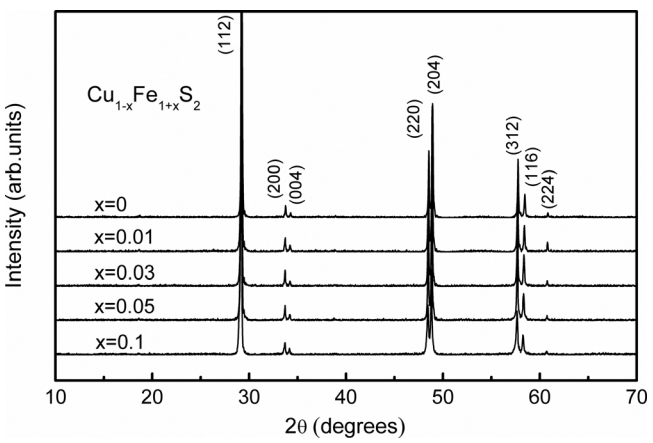

FIG. 1. XRD patterns for $Cu_{1-x}Fe_{1+x}S_2$.

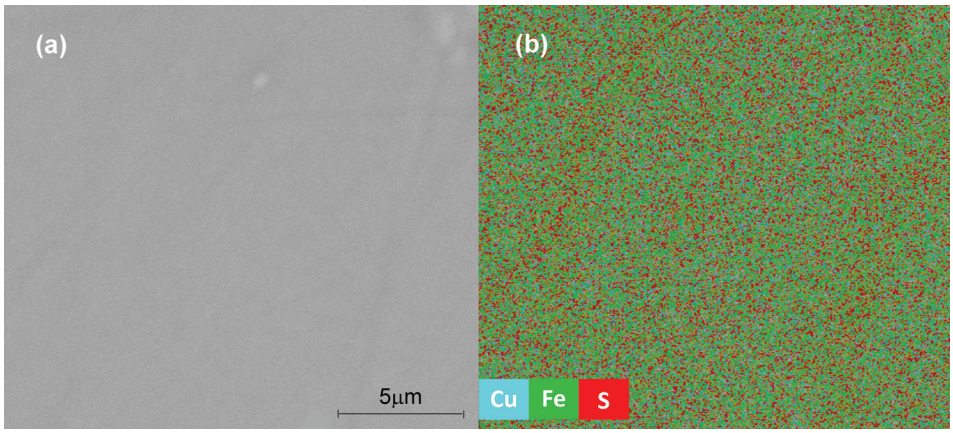

FIG. 2. (a) BSE image of the polished surface and (b) x-ray map by EDS for sample $Cu_{0.9}Fe_{1.1}S_2$.

TABLE I. Nominal compositions, atom ratio of Fe/Cu based on the EDS measurement, volume of unit cell V, band gap E_g, and room temperature lattice thermal conductivity κ_L, electrical conductivity σ, Seebeck coefficient α, Hall carrier concentration n, Hall mobility μ_H in $Cu_{1-x}Fe_{1+x}S_2$.

Nominal Composition	Fe/Cu (atomic ratio)	V (a^2c) (Å^3)	κ_L (W/mK)	σ ($10^4\ \Omega^{-1}\ m^{-1}$)	α (μV/K)	n (10^{20} cm^{-3})	μ_H (cm^2/Vs)	E_g (eV)
$CuFeS_2$	1.005	291.75	5.9	0.25	−370	0.34	3.0	0.34
$Cu_{0.99}Fe_{1.01}S_2$	1.020	292.04	5.7	0.74	−307	0.75	5.1	0.36
$Cu_{0.97}Fe_{1.03}S_2$	1.102	292.30	4.2	1.45	−224	2.11	3.6	0.32
$Cu_{0.95}Fe_{1.05}S_2$	1.132	292.68	3.8	1.95	−189	3.42	3.3	0.29
$Cu_{0.9}Fe_{1.1}S_2$	1.175	292.74	3.2	2.11	−139	7.02	1.7	0.19

conductivity increases with increasing Fe doping content while the absolute value of Seebeck coefficient decreases. The detailed mechanisms will be discussed below. All samples exhibit negative Seebeck coefficients in the whole measured temperature range, indicating n-type materials with electrons as the charge carriers. When temperature is increasing, the absolute values of Seebeck coefficient increase first and then decline due to thermal excitation of carriers. This indicates these samples could be treated as intrinsic semiconductors at high temperatures. For an intrinsic semiconductor, both electrons and holes contribute to the electrical transport and they make opposite contributions to the total Seebeck coefficient. Thus reduced Seebeck coefficients are expected, which can be described by[25]

$$\alpha = \frac{\alpha_e\sigma_e + \alpha_h\sigma_h}{\sigma_e + \sigma_h}, \tag{1}$$

where the subscript symbols e and h represent electron and hole, respectively.

For sample $CuFeS_2$, the intrinsically thermal excitation occurs at 400 K, which indicates a relatively small band gap (E_g). The E_g can be estimated by[25]

$$E_g = 2e\alpha_{max}T_{max}, \tag{2}$$

where e is the electron charge, α_{max} is the maximum value of Seebeck coefficient, and T_{max} is the temperature at which the maximum thermopower occurs. The estimated E_g for $CuFeS_2$ is about 0.34 eV, in agreement with the calculated 0.3 eV in Ref. 19, but smaller than the value by optical absorption measurement.[18] With increasing Fe doping content, the T_{max} moves towards high temperature gradually except for the sample with $x = 0.1$.

Like other high thermoelectric performance diamond-like compounds, $Cu_{1-x}Fe_{1+x}S_2$ also shows relatively low thermal conductivity due to the highly distorted crystal structures, especially at high temperature, as shown in Figure 4. The thermal conductivity is reduced dramatically with increasing temperatures. This is similar to those in almost all

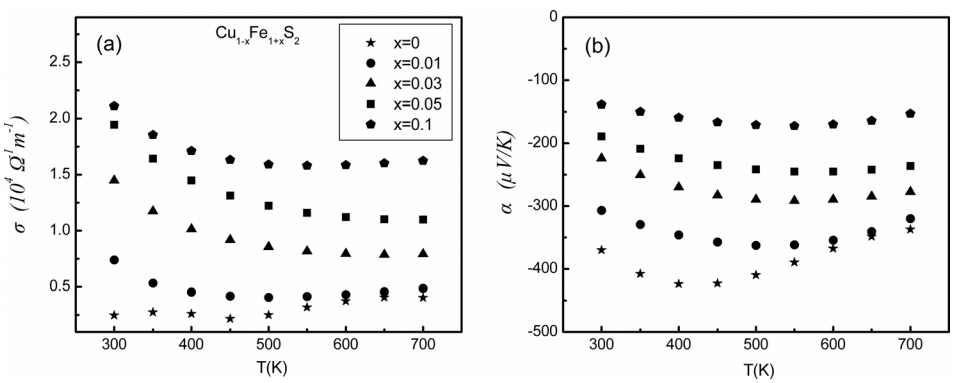

FIG. 3. Temperature dependence of (a) electrical conductivity σ and (b) Seebeck coefficient α for $Cu_{1-x}Fe_{1+x}S_2$ samples (300∼700 K).

diamond-like compounds due to strong phonon Umklapp scattering at high temperatures. In addition, the thermal conductivity is decreases significantly with increasing Fe/Cu atomic ratios in the entire temperature range. This could be due to the extra lattice defects between the Fe and Cu atoms and the details will be discussed in Sec. III D. The minimum value of thermal conductivity for $Cu_{0.9}Fe_{1.1}S_2$ is about 1 W/m·K at 700 K, a quite low value in the diamond-like compounds. Fig. 4 also lists the thermal conductivity of other typical diamond-like compounds. $CuFeS_2$-based materials show lower thermal conductivity than those in other ternary compounds such as $CuInTe_2$ and $CuGaTe_2$. Even compared with the thermal conductivity of quaternary compounds, $CuFeS_2$-based materials with large Fe/Cu atomic ratios still show lower values at high temperatures.[13–16]

Figure 5 shows the temperature dependence of the figure of merit zT ($=\alpha^2\sigma T/\kappa$) from 300 to 700 K for $Cu_{1-x}Fe_{1+x}S_2$. The zT values of the reported $CuFeS_2$-based compounds from reference 22 and 23 are also plotted in Figure 5 for a comparison. With the increase of temperature, the zT values increase monotonically for all $Cu_{1-x}Fe_{1+x}S_2$ samples and there is no indication of reaching a maximum value at 700 K. As a result of tuned electrical properties and suppressed thermal conductivity by enlarging the Fe/Cu atomic ratios, the zT value is much improved, more than 50% enhancement in sample $Cu_{0.97}Fe_{1.03}S_2$ and $Cu_{0.95}Fe_{1.05}S_2$ at 700 K compared with $CuFeS_2$. When the Fe content is 3% excess, chalcopyrite $Cu_{1-x}Fe_{1+x}S_2$ material exhibits a maximum zT value of about 0.33 at 700 K. Further optimization such as other doping with other elements could further reduce the thermal conductivity and enhance electrical properties for the realization of high thermoelectric performance in such a Cu-Fe-S compound with earth-abundant, non-toxic, and inexpensive elements.

C. Electrical transport properties

Hall carrier concentration (n) versus Fe doping content (x) at room temperature for $Cu_{1-x}Fe_{1+x}S_2$ is plotted in Figure 6. By excessive Fe substituted at Cu sites, the electron concentration is significantly increased and a nice linear dependence

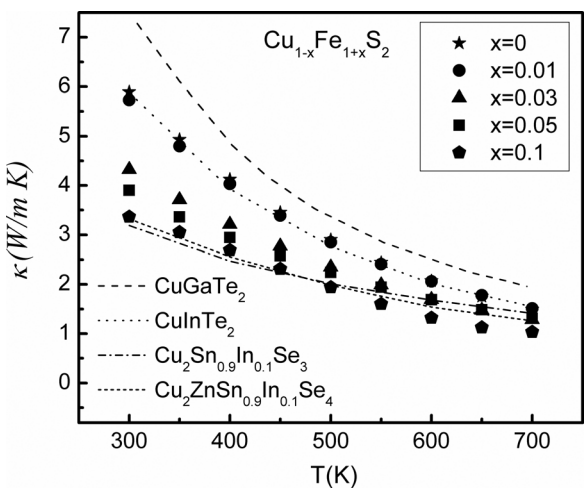

FIG. 4. Temperature dependence of thermal conductivity (κ) for $Cu_{1-x}Fe_{1+x}S_2$. The data for other diamond-like compounds from literature 13–16 are also listed for data comparison.[13–16]

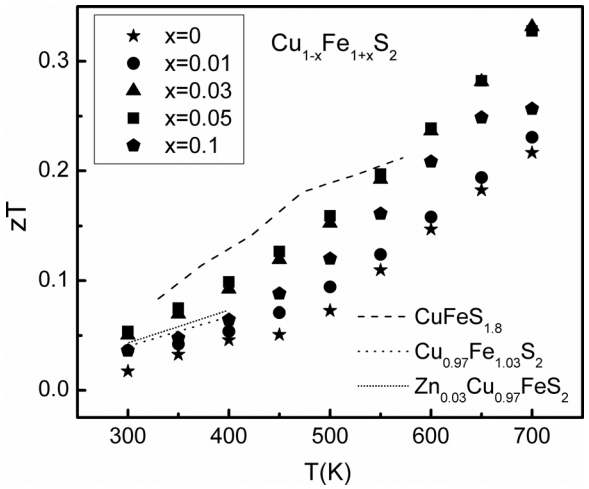

FIG. 5. Temperature dependence of zT for $Cu_{1-x}Fe_{1+x}S_2$ (300~700 K). The data for the reported $CuFeS_2$-based compounds are listed for data comparison.[22,23]

is observed in Fig. 6. The room temperature carrier concentration values are changed in a wide range from 3.4×10^{19} cm^{-3} to 7×10^{20} cm^{-3}, indicating that Fe is an effective dopant at the Cu site. In $CuFeS_2$, the charge state of S is usually treated as 2^-. The charge states of Cu and Fe are still open questions. The measured and calculated results of the magnetic moment show that the electron states of $CuFeS_2$ are a commixture of $Cu^+Fe^{3+}S^{2-}{}_2$ and $Cu^{2+}Fe^{2+}S^{2-}{}_2$.[19,26] The enhanced electron concentration by extra Fe substituted at Cu sites indicates that Fe donates more valence electrons than Cu. Therefore, the charge states of Cu and Fe in $CuFeS_2$ could be +1 and +3.

The temperature dependence of Hall mobility (μ_H) for all the samples is shown in Figure 7. The room temperature Hall mobility of doped samples decreases from 5 to 1.7 cm^2/V·s with increasing Fe content. These values are comparable to the literature data.[23] For pure $CuFeS_2$ (x = 0), the Hall mobility follows a $T^{3/2}$ dependence indicative of ionized impurities dominated carrier scattering. The ionized impurities in $CuFeS_2$ lattice generate a long range Coulomb potential field to scatter electrons strongly, leading to the very low mobility

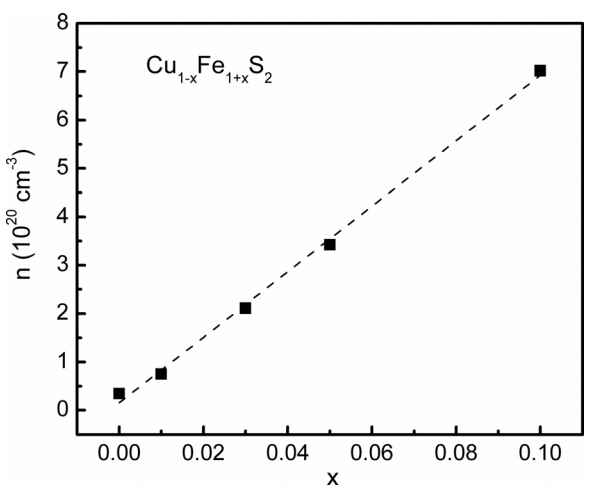

FIG. 6. Hall carrier concentration (n) as a function of doping content (x) at room temperature for $Cu_{1-x}Fe_{1+x}S_2$. The dashed line is a guide to the eyes.

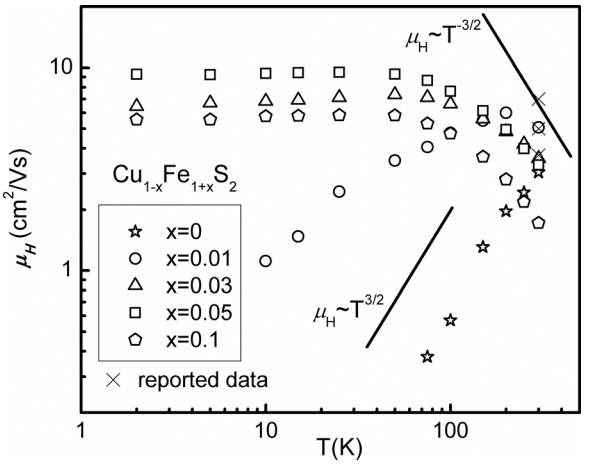

FIG. 7. Temperature dependence of Hall mobility (μ_H) for $Cu_{1-x}Fe_{1+x}S_2$. The crosses are the reported data from literature 23. The $T^{3/2}$ and $T^{-3/2}$ relationships are also presented.

of $CuFeS_2$ throughout the whole temperature range investigated. With the increase of Fe content, the temperature dependence of Hall mobility approaches to $\mu_H \sim T^{-3/2}$ near room temperature in the samples with high carrier concentrations (x = 0.03, 0.05, 0.1), indicating acoustic phonon scatterings start dominating carrier scattering mechanism.[27,28] At temperatures below 50 K the Hall mobility tends towards a constant value, suggestive of neutral impurity scattering. For the 1% Fe doped sample (x = 0.01), the temperature dependence of mobility and is more flat at both high and low temperature. This behavior reveals a combination of carrier scattering mechanisms including both acoustic phonons and ionized impurities dominated mechanisms.

With the increase of Fe doping content, the positions of the Fermi level and the variations of the band structure can be inferred roughly from the carrier effective mass. We estimated the electron effective masses of $Cu_{1-x}Fe_{1+x}S_2$ using the single parabolic band model. In this model, the Seebeck coefficient α and the carrier concentration n are expressed as

$$\alpha = \frac{k_B}{e}\left(\frac{(2+\Lambda)F_{\Lambda+1}(\psi)}{(1+\Lambda)F_{\Lambda}(\psi)} - \psi\right), \tag{3}$$

$$n = \frac{4\pi(2m*k_BT)^{3/2}}{h^3}F_{1/2}(\psi), \tag{4}$$

where k_B is the Boltzmann constant, h is the Planck constant, e is elementary charge, m^* is the effective mass, ψ is the reduced Fermi level, $F_j(\psi)$ is the Fermi integral of order j, and Λ is a scattering parameter related to the energy dependence of the carrier scattering mechanism. The value of Λ is 0 when the acoustic phonon scattering, or 2 when the ionized impurity scattering.[29,30] The effective mass can be calculated from the experimental values of the Seebeck coefficient and the carrier concentration using Eqs. (3) and (4). Λ of 2 is applied to calculate the effective mass of the sample $CuFeS_2$ (x = 0) due to the ionized impurities dominated carrier scattering. For the high carrier concentration samples (x = 0.03, 0.05, 0.1), Λ of 0 is used, because dominant carrier scattering mechanism is acoustic phonon scattering. For a comparison, Λ of 1 and 2 are applied to calculate the effective mass of the 1% Fe doped sample (x = 0.01), respectively. Due to the mixed carrier scattering mechanism in $Cu_{0.99}Fe_{1.01}S_2$, the result using $\Lambda = 1$ should be closer to the truth. Figure 8 illustrates the calculated effective mass (m^*) as a function of carrier concentration for $Cu_{1-x}Fe_{1+x}S_2$. The effective masses of all the samples are very large, consistent with the calculated heavy effective mass by Naohito Tsujii and Takao Mori,[23] as shown in Fig. 8, suggestive of relatively large density of state (DOS) near Fermi level. The large density of states could lead to large Seebeck coefficient, but the carrier mobility is also strongly affected to show very low values with the motility data shown in Fig. 7. With the increase of Fe content, the effective mass increases notably, from 1.2 m_0 to 5.6m_0 (m_0 is the free electron mass), indicating that Fe substituted on the Cu site has a strong influence on the band structure around Fermi level. According to the calculated band structure of $CuFeS_2$ by Hamajima *et al.*, the bands around Fermi level are composed mainly of the 3d orbital of Fe, which means that the electrical properties of $CuFeS_2$ will be relevant to the 3d valence electron of Fe.[19] Therefore, exactly as the results of effective mass exhibited, the addition of Fe will affect strongly the band structure of $CuFeS_2$.

Figure 9(a) displays the room temperature power factor ($\alpha^2\sigma$) as a function of carrier concentration (n) for $Cu_{1-x}Fe_{1+x}S_2$ and the reported data of $CuFeS_2$-based compounds. In our samples, the best power factors are in the range of 7 to 7.3 $\times$ 10^{-4} W/mK^2 for the samples with x between 0.01 and 0.05. Although the power factors in our samples are slightly lower than the value from Tsujii *et al.*, all these samples show a clear trend in the relationship between the power factors and carrier concentrations.[23] The optimum carrier concentration for $CuFeS_2$-based diamond-like compounds is in the range from 1 to 3 $\times$ 10^{20} cm^{-3}. In tetrahedral diamond-like compounds, Zhang *et al.* reveals the unity-η rule to explain and predict the electrical transport

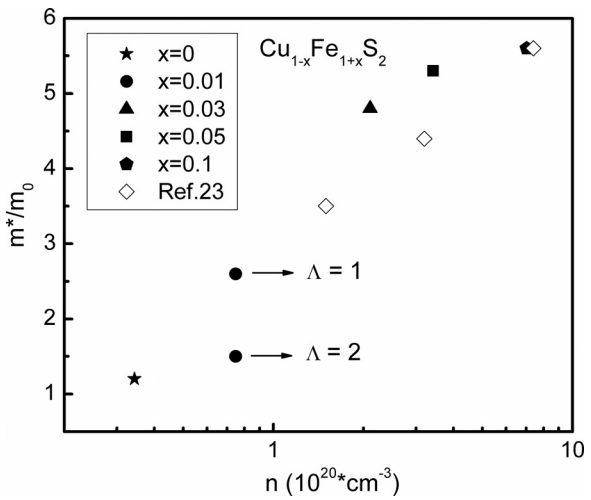

FIG. 8. The electron effective mass (m^*) as a function of carrier concentration (n) for $Cu_{1-x}Fe_{1+x}S_2$ at room temperature. Due to the different carrier scattering mechanisms in $Cu_{1-x}Fe_{1+x}S_2$, the Λ of 0 is used for the samples with x = 0.03, 0.05, 0.1, Λ of 2 is used for the sample $CuFeS_2$ (x = 0), and Λ of 1 and 2 are used for the sample with x = 0.01 (black points in the Fig. 8). The literature data are plotted for a comparison.[23]

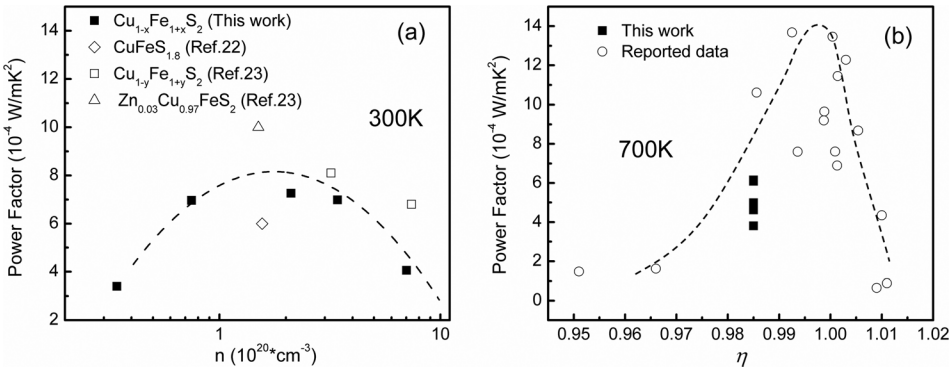

FIG. 9. (a) Room temperature power factor ($\alpha^2\sigma$) as a function of carrier concentration (n) for $Cu_{1-x}Fe_{1+x}S_2$. The literature data are also shown in the figure.[22,23] (b) Power factors ($\alpha^2\sigma$) as a function of tetragonal distortion parameter (η) for $Cu_{1-x}Fe_{1+x}S_2$ and other tetrahedral diamond-like compounds at 700 K.[17] The dashed lines are guide to the eyes.

properties.[17] Figure 9(b) shows the power factor at 700 K as a function of tetragonal distortion parameter (η) for our $Cu_{1-x}Fe_{1+x}S_2$ with the estimated trend based on the typically tetrahedral diamond-like compounds. Although $CuFeS_2$ has a η value that deviates from unity more than $CuInTe_2$ or $CuGaTe_2$, which leads to low power factors, it is exciting that all our data are below the general trend and the highest power factor is just below the usual curve in tetrahedral diamond-like compounds. This means that our data are fully consistent with theoretical model by Zhang *et al.* because the estimated curve shown in Fig. 9(b) is the maximum power factor that tetrahedral diamond-like materials can reach.

D. Thermal conductivity

Figure 10 shows the low-temperature thermal conductivity (κ) and lattice thermal conductivity (κ_L) from 4 to 300 K for all $Cu_{1-x}Fe_{1+x}S_2$ samples. The room temperature thermal conductivities of the Cu-site doped $CuFeS_2$ in literatures are plotted for a comparison.[23,24] The total thermal conductivity consists of carrier thermal conductivity (κ_e) and lattice thermal conductivity (κ_L), written as $\kappa = \kappa_e + \kappa_L$. κ_e is estimated using the Wiedemann-Franz law with a constant Lorentz number $L_0 = 2.0\times10^{-8}$ V^2/K^2. κ_L is obtained by subtracting κ_e from κ. Due to the small magnitude of electrical conductivity, the carrier contribution to the total thermal conductivity is very small. In this case, it is reasonable to choose a constant Lorentz number in the calculation of κ_e. As expected, the κ_L values and its temperature dependence are similar to those of total thermal conductivity. This implies that lattice phonon scattering dominating heat conduction in $Cu_{1-x}Fe_{1+x}S_2$.

When increasing the Fe content, the room temperature κ_L is depressed up to 48%, which indicates the non-stoichiometric Cu/Fe ratios strongly enhance the phonon scattering. In order to clarify the role of the non-stoichiometric Cu/Fe ratios in suppression of the heat transport, the Debye approximation is used to model the temperature dependence of the lattice thermal conductivity for all the samples at low temperature. In the Debye model, lattice thermal conductivity is given by[31,32]

$$\kappa_L = \frac{k_B}{2\pi^2 v}\left(\frac{k_B}{\hbar}\right)^3 T^3 \int_0^{\theta_D/T} \frac{x^4 e^x}{\tau_c^{-1}(e^x-1)^2}\,dx, \qquad (5)$$

where $x = \hbar\omega/k_BT$, ω is the phonon frequency, k_B is the Boltzmann constant, $\hbar$ is the reduced Planck constant, θ_D is the Debye temperature, v is the velocity of sound, and τ_c is the phonon scattering relaxation time. The overall phonon scattering relaxation rate τ_c^{-1} is written as

$$\tau_c^{-1} = \tau_B^{-1} + \tau_D^{-1} + \tau_U^{-1} = \frac{v}{L} + A\omega^4 + B\omega^2 T e^{-\theta_D/3T}, \qquad (6)$$

where τ_B, τ_D, and τ_U are the relaxation times for grain boundary scattering, point defect scattering and phonon-phonon Umklapp scattering, respectively. And L is the grain size, the coefficients A (point defect scattering) and B (Umklapp scattering) are the fitting parameters. In our calculations, the Debye temperature (θ_D) is 263 K taken from literature,[33] and the velocity of sound (v) is 2938 m/s. This is the averaged value of our $Cu_{1-x}Fe_{1+x}S_2$ samples excluding sample $Cu_{0.9}Fe_{1.1}S_2$ because of its large deviation from the averaged value. The averaged velocity of sound (v_{ave}) for each sample is calculated by the equation $v_{ave} = (1/3v_l^3 + 2/3v_s^3)^{1/3}$, where v_l and v_s are longitudinal and shear velocity of sound,

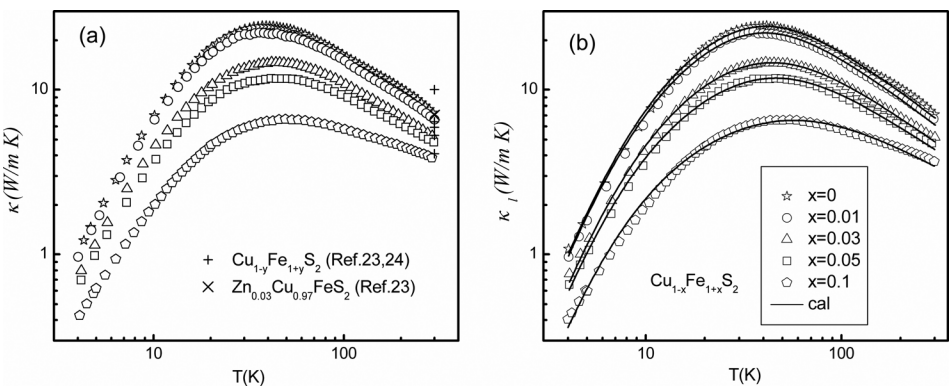

FIG. 10. Low-temperature (a) thermal conductivity κ and (b) lattice thermal conductivity κ_L from 4 to 300 K for $Cu_{1-x}Fe_{1+x}S_2$. The data for Cu-site doped $CuFeS_2$ in Refs. 23 and 24 are plotted for a comparison. The solid lines in (b) are calculated curves based on Eqs. (5) and (6).

TABLE II. Fitted parameter *L*, *A*, *B*, Γ_{exp}, Γ_{mass}, and Γ_{strain} by Eqs. (5)–(8), and longitudinal (v_l), shear (v_s), and averaged (v_{ave}) velocity of sound for $Cu_{1-x}Fe_{1+x}S_2$.

x	L (μm)	A (10^{-43} s^3)	B(10^{-18} s/K)	Γ_{exp} (10^{-3})	Γ_{mass} (10^{-3})	Γ_{strain} (10^{-3})	v_l (m/s)	v_s (m/s)	v_{ave} (m/s)
0	3.825	11.327	3.396	…	…	…	3764	2056	2867
0.01	3.717	12.878	3.713	5.985	0.07	5.915	4227	2122	3159
0.03	2.519	21.29	4.195	9.895	0.206	9.689	3650	1950	2765
0.05	2.34	29.728	4.2	13.77	0.339	13.431	3916	2065	2958
0.1	1.505	65.523	3.557	30.35	0.65	29.7	3256	1829	2497

respectively. The longitudinal (v_l), shear (v_s), and average (v_{ave}) velocity of sound for all $Cu_{1-x}Fe_{1+x}S_2$ samples are listed in Table II.

Figure 10(b) plots the fitted curves of lattice thermal conductivity for all $Cu_{1-x}Fe_{1+x}S_2$ samples using Eqs. (5) and (6). The solid lines fit the experimental data very well over the entire temperature range for all five samples, indicating that $Cu_{1-x}Fe_{1+x}S_2$ is describable in terms of phonon scattering by boundaries, defects, and Umklapp processes. Table II lists the fitted parameters. The grain size (L) varies from about 1.5 to 4 μm, consistent with the results, ranging from 1 to 20 μm observed by SEM. For Umklapp scattering, the prefactor B is about 4×10^{-18} s/K for all the samples and no obvious trend as a function of x is observed. However, the coefficient A for point defect scattering increases notably with increasing doping content as shown in Figure 11. This means the phonon-point defect scattering is strongly enhanced by Fe replacement on the Cu site, which suppresses the lattice thermal conductivity remarkably.

For exploring the origin of point defect scattering, the coefficient A is defined as[32,34]

$$A = \frac{\Omega_0}{4\pi v^3}\Gamma_{exp}, \tag{7}$$

where Ω_0 is the volume of the primitive cell and Γ_{exp} is an experimental disorder scattering parameter. For $CuFeS_2$, Ω_0 equals to $V/4$, where V is the volume of unit cell and list in Table I. In general, point defect scattering is a sum of two contributions: mass fluctuation deriving from the mass difference between the impurity atom and the matrix atom, and strain field fluctuation due to the difference of atom size and interatomic coupling force.[35] Thus, Γ_{exp} can be written as $\Gamma_{exp} = \Gamma_{mass} + \Gamma_{strain}$, where Γ_{mass} and Γ_{strain} are scattering parameters concerning mass fluctuation and strain field fluctuation, respectively. For a ternary compound $U_uV_vW_w$, the Γ_{mass} is given by[10,36]

$$\Gamma_{mass}(U_uV_vW_w) = \frac{u\left(\frac{M_u}{M_m}\right)^2\Gamma(U) + v\left(\frac{M_v}{M_m}\right)^2\Gamma(V) + w\left(\frac{M_w}{M_m}\right)^2\Gamma(W)}{u+v+w}, \tag{8}$$

where $M_m = (uM_u + vM_v + wM_w)/(u+v+w)$. For $Cu_{1-x}Fe_{1+x}S_2$, U = (Cu, Fe), V = Fe, and W = S. For a simple type of impurity atom with a concentration of ϕ, the scattering parameter is given by $\Gamma = \phi(1-\phi)(\Delta M/M_{av})^2$, with $\Delta M = M_i - M_h$ and $M_{av} = \phi M_i + (1-\phi)M_h$, where M_i and M_h are the masses of the impurity and host atoms, respectively. The Γ_{strain} is obtained by subtracting Γ_{mass} from Γ_{exp}. The calculated scattering parameters list in Table II, and Γ_{exp} and Γ_{mass} as a function of x are plotted in Figure 12. As shown, the contributions of mass fluctuation to phonon-point defect scattering are small because the mass difference between Cu and Fe is only 10%. Whereas, the values of Γ_{strain} are much larger than the Γ_{mass}, which demonstrates that the strain field fluctuation introduced by alloying Fe on the Cu sub-lattice is the major contribution to phonon-point

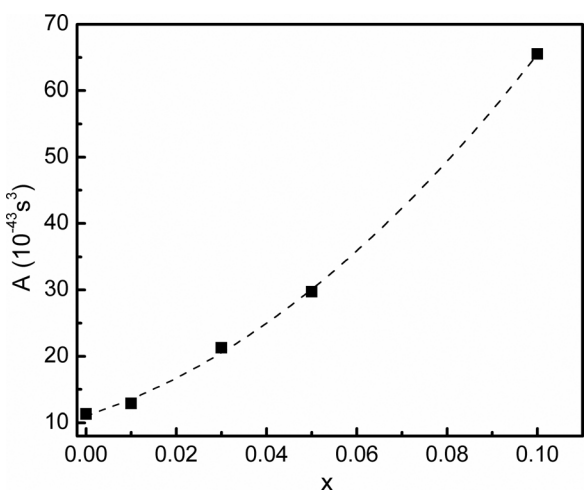

FIG. 11. Coefficient A as a function of doping content (x). The dashed line is a guide to the eyes.

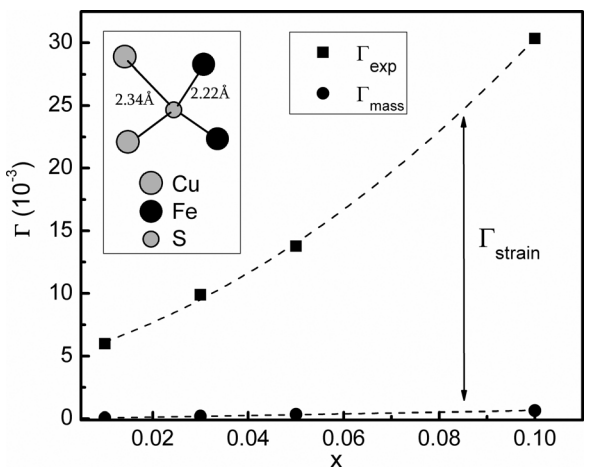

FIG. 12. Parameter Γ_{exp} and Γ_{mass} as a function of doping content (x). The dashed lines are guides to the eyes. The insert figure shows the bonded Cu-Fe-S tetrahedron in the lattice of $CuFeS_2$. The bond length of 2.34 Å for Cu-S bond and 2.22 Å for Fe-S bond are labeled.

defect scattering, leading to the much lowered lattice thermal conductivity.

In the lattice of $CuFeS_2$, two Fe atoms and two Cu atoms bond to a sulfur atom to form a Cu-Fe-S tetrahedron unit as shown in Figure 12. However, the sulfur atom displaces from the center of the bonded tetrahedron, arising that the Fe-S bond is stronger and more anisotropic than the Cu-S bond. The calculated bond lengths of 2.34 Å for the Cu-S bond and 2.22 Å for the Fe-S bond by Jaffe and Zunger are labeled in Figure 12.[37] When one Cu atom is replaced by an extra Fe atom, the S atom will further deviate from the center of the tetrahedron toward the final Cu atom, leading to an extra local distortion. The large differences in the coupling force to the sulfur atom between Fe and Cu atoms are expected to give rise to the strong strain fluctuation contributing to phonon scattering. Such a strong strain contribution from Fe substitution was demonstrated in $Cu_2Zn_{1-x}Fe_xGeSe_4$.[38]

IV. CONCLUSION

We have investigated the thermoelectric properties of Fe doped chalcopyrite $Cu_{1-x}Fe_{1+x}S_2$ ($x = 0$, 0.01, 0.03, 0.05, 0.1), which were prepared through a melting-annealing-sintering process. All the elements are homogeneously distributed in the samples without obvious impurity phases. With Fe doping on the Cu site, the electron concentration is tuned in a wide range from $3.4\times10^{19}\,cm^{-3}$ to $7\times10^{20}\,cm^{-3}$ at room temperature, indicating Fe is an effective n-type dopant. The electrical properties follow well the general trend in tetrahedral diamond-like compounds and the optimum carrier concentration is estimated based on our data. We also modeled the much reduced low-temperature thermal conductivity. The disordered ion Cu/Fe distributions introduce large strain field fluctuation into the crystal lattice, leading to significantly enhanced phonon-point defect scattering. Optimized power factor and depressed thermal conductivity result in much improved zT values, more than 50% enhancement at 700 K, due to approach to the optimum carrier concentration and lowered lattice thermal conductivity by the Fe dopant.

ACKNOWLEDGMENTS

This work was supported by National Basic Research Program of China (973-program) under Project No. 2013CB632501, and National Natural Science Foundation of China (NSFC) under the Nos. 11234012 and 51121064, and the AFOSR MURI program.

[1]D. M. Rowe, *CRC Handbook of Thermoelectrics* (CRC Press, Boca Raton, 1995).
[2]L. E. Bell, Science **321**, 1457 (2008).
[3]G. J. Snyder and E. S. Toberer, Nat. Mater. **7**, 105 (2008).
[4]B. Poudel, Q. Hao, Y. Ma, Y. Lan, A. Minnich, B. Yu, X. Yan, D. Wang, A. Muto, D. Vashaee, X. Chen, J. Liu, M. S. Dresselhaus, G. Chen, and Z. Ren, Science **320**, 634 (2008).
[5]K. F. Hsu, S. Loo, F. Guo, W. Chen, J. S. Dyck, C. Uher, T. Hogan, E. K. Polychroniadis, and M. G. Kanatzidis, Science **303**, 818 (2004).
[6]K. Biswas, J. He, I. D. Blum, C. Wu, T. P. Hogan, D. N. Seidman, V. P. Dravid, and M. G. Kanatzidis, Nature **489**, 414 (2012).
[7]B. C. Sales, D. Mandrus, and R. K. Williams, Science **272**, 1325 (1996).
[8]X. Shi, J. Yang, J. R. Salvador, M. Chi, Jung Y. Cho, H. Wang, S. Bai, J. Yang, W. Zhang, and L. Chen, J. Am. Chem. Soc. **133**, 7837 (2011).
[9]X. Shi, J. Yang, S. Bai, J. Yang, H. Wang, M. Chi, J. R. Salvador, W. Zhang, L. Chen, and W. Wong-Ng, Adv. Funct. Mater. **20**, 755 (2010).
[10]H. Liu, X. Shi, F. Xu, L. Zhang, W. Zhang, L. Chen, Q. Li, C. Uher, T. Day, and G. J. Snyder, Nat. Mater. **11**, 422 (2012).
[11]Y. He, T. Day, T. Zhang, H. Liu, X. Shi, L. Chen, and G. J. Snyder, Adv. Mater. **26**, 3974 (2014).
[12]X. Lu, D. T. Morelli, Y. Xia, F. Zhou, V. Ozolins, H. Chi, X. Zhou, and C. Uher, Adv. Energy Mater. **3**, 342 (2013).
[13]X. Y. Shi, F. Q. Huang, M. L. Liu, and L. D. Chen, Appl. Phys. Lett. **94**, 122103 (2009).
[14]X. Shi, L. Xi, J. Fan, W. Zhang, and L. Chen, Chem. Mater **22**, 6029 (2010).
[15]R. Liu, L. Xi, H. Liu, X. Shi, W. Zhang, and L. Chen, Chem, Commun. **48**, 3818 (2012).
[16]T. Plirdpring, K. Kurosaki, A. Kosuga, T. Day, S. Firdosy, V. Ravi, G. J. Snyder, A. Harnwunggmoung, T. Sugahara, Y. Ohishi, H. Muta, and S. Yamanaka, Adv. Mater. **24**, 3622 (2012).
[17]J. Zhang, R. Liu, N. Cheng, Y. Zhang, J. Yang, C. Uher, X. Shi, L. Chen, and W. Zhang, Adv. Mater. **26**, 3848 (2014).
[18]I. G. Austin, C. H. L. Goodman, and A. E. Pengelly, Nature **178**, 433 (1956).
[19]T. Hamajima, T. Kambara, and K. I. Gondaira, Phys. Rev. B **24**, 3349 (1981).
[20]T. Teranishi, J. Phys. Soc. Jpn. **16**, 1881 (1961).
[21]B. Donovan and G. Reichenbaum, Br. J. Appl. Phys. **9**, 474 (1958).
[22]J. Li, Q. Tan, and J. Li, J. Alloys Compd. **551**, 143 (2013).
[23]N. Tsujii and T. Mori, Appl. Phys. Express **6**, 043001 (2013).
[24]N. Tsujii, J. Electron. Mater. **42**, 1974 (2013).
[25]H. J. Goldsmid and J. W. Sharp, J. Electron. Mater. **28**, 869 (1999).
[26]G. Donnay, L. M. Corliss, J. D. H. Donnay, N. Elliott, and J. M. Hastings, Phys. Rev. **112**, 1917 (1958).
[27]N. Cheng, R. H. Liu, S. Q. Bai, X. Shi, and L. D. Chen, J. Appl. Phys. **115**, 163705 (2014).
[28]B. M. Askerov, *Electron Transport Phenomena in Semiconductors* (World Scientific Publishing Co. Pte. Ltd., 1994).
[29]J. Bardeen and W. Shockley, Phys. Rev. **80**, 72 (1950).
[30]E. Conwell and V. F. Weisskopf, Phys. Rev. **77**, 388 (1950).
[31]J. Callaway, Phys. Rev. **113**, 1046 (1959).
[32]J. Callaway and H. C. Baeyer, Phys. Rev. **120**, 1149 (1960).
[33]H. N. Ok, K. S. Back, and E. J. Choi, Phys. Rev. B **50**, 10327 (1994).
[34]P. G. Klemens, Proc. Phys. Soc. A **68**, 1113 (1955).
[35]B. Abeles, Phys. Rev. **131**, 1906 (1963).
[36]G. A. Slack, Phys. Rev. **126**, 427 (1962).
[37]J. E. Jaffe and A. Zunger, Phys. Rev. B **29**, 1882 (1984).
[38]W. G. Zeier, Y. Pei, G. Pomrehn, T. Day, N. Heinz, C. P. Heinrich, G. J. Snyder, and W. Tremel, J. Am. Chem. Soc. **135**, 726 (2013).